Influence of temperature and bias voltage on the performance of a high resolution PET detector built with position sensitive avalanche photodiodes

2012 JINST 7 P08001

(http://iopscience.iop.org/1748-0221/7/08/P08001)

PUBLISHED BY IOP PUBLISHING FOR SISSA MEDIALAB

RECEIVED: *March 15, 2012*
REVISED: *June 4, 2012*
ACCEPTED: *June 22, 2012*
PUBLISHED: *August 1, 2012*

2012 JINST 7 P08001

Influence of temperature and bias voltage on the performance of a high resolution PET detector built with position sensitive avalanche photodiodes

A. Vandenbroucke,[a,1] **T.J. McLaughlin**[b] **and C.S. Levin**[a,b,c]

[a]*Molecular Imaging Program at Stanford, Dept. of Radiology, Stanford, CA, U.S.A.*
[b]*Department of Physics, Stanford, CA, U.S.A.*
[c]*Departments of Electrical Engineering and Bioengineering, Stanford, CA, U.S.A.*

E-mail: arnevdb@stanford.edu

[1]Corresponding author

doi:10.1088/1748-0221/7/08/P08001

ABSTRACT: We evaluate the performance of an 8×8 array of $0.9 \times 0.9 \times 1$ mm^3 cerium doped lutetium oxyothosilicate (LSO) crystals coupled to a position sensitive avalanche photodiode (PSAPD) as a function of bias voltage and temperature. We use this detector to develop a general methodology to optimize bias voltage, temperature, and gain for PET detectors using semiconductor photodetectors. This detector module will be used in a novel high resolution positron emission tomography (PET) camera dedicated to breast imaging under construction in our lab. Due to the tight packing of many PSAPDs in the system a thermal gradient is expected across the imaging heads.

Data were collected for 11 PSAPD temperatures between 5°C and 40°C using a thermoelectric (Peltier) device. At each temperature the bias voltage was varied in steps of 5 V over a 50 V range. We present three methods to predict the optimal bias voltage at every temperature: one based on optimizing the coincidence time resolution, the others based on the relative change in PSAPD gain and leakage current due to the onset of hole multiplication. Optimal gain could also be predicted based on the quality of the flood histogram.

At optimal bias voltage, the energy resolution degrades as $(10.5 \pm 0.1) + \big((0.038 \pm 0.006)\,/\,{}^{\circ}C \cdot \mathrm{T}\big)\%$. Time resolution stays constant at 2.37 ± 0.02 ns below 15°C. Above this temperature, time resolution deteriorates as $(1.67 \pm 0.06) + ((0.042 \pm 0.002)\,/{}^{\circ}C \cdot \mathrm{T})$ ns. Even at high temperatures, all 64 crystal position peaks in the flood histogram are still clearly visible. The width of the peaks in the flood histogram show a quadratic degradation with temperature: $(2.6 \pm 0.1) \cdot 10^{-2} + (1.6 \pm 0.2) \cdot 10^{-5}/({}^{\circ}C)^2 \cdot \mathrm{T}^2$.

We conclude that both the quality of the flood histogram as well as the coincidence time resolution are better parameters to estimate the optimal bias voltage, than energy resolution. Optimal bias voltage is found to be dependent on the value of *k*, the ratio between hole and electron multiplication. We achieve optimal bias at a similar gain at all temperatures. The optimal bias voltage changes linearly across the observed range.

KEYWORDS: Photon detectors for UV, visible and IR photons (solid-state) (PIN diodes, APDs, Si-PMTs, G-APDs, CCDs, EBCCDs, EMCCDs etc); Scintillators, scintillation and light emission processes (solid, gas and liquid scintillators); Gamma camera, SPECT, PET PET/CT, coronary CT angiography (CTA)

2012 JINST 7 P08001

Contents

2012 JINST 7 P08001

1 Introduction

Silicon semiconductor photodetectors such as avalanche photodiodes (APD) and silicon photomultipliers (SiPM) have gained much interest for the use in the newest generation small animal and whole body Positron Emission Tomography (PET) cameras [1–4]. Their compact form factor and the insensitivity to magnetic fields are advantageous compared to more traditional photo multiplier tubes (PMT). It is well known that the behavior of both APDs and SiPMs are strongly dependent on both bias voltage and temperature. For APDs, the analog pulse shape is directly affected, while for SiPMs changes in photon detection efficiency, optical cross talk and dark noise affect count rate and timing performance. In general, due to a reduction in thermally generated electron hole pairs (i.e. leakage current), we expect an improved performance at lower temperatures. This paper

quantifies performance based on gain, energy resolution, coincidence timing resolution, leakage current, and the quality of the flood histogram as a function of both temperature and bias voltage of a high resolution PET detector based on position sensitive avalanche photodiodes (PSAPD).

Data was collected using an 8×8 array of $1 \times 1 \times 1$ mm^3 Lutetium Oxyorthosilicate (LSO) crystals coupled to PSAPD chips. It is expected that the optimal bias voltage is temperature dependent, and we aim to find the 'best' bias voltage at every temperature. These LSO-PSAPD modules under study are to be used in a novel 1 mm^3 resolution, high sensitivity PET scanner for breast imaging [5–7]. The system is designed with a new concept for a position sensitive PET detector intended to provide a uniform intrinsic spatial resolution of 1 mm^3, high scintillation light collection efficiency, directly measured photon depth of interaction (DOI), and the ability to position individual coordinates of multi-interaction photon events in three dimensions (3-D) [8–11]. The modules will be arranged in registration cards [12] which will cause a 4°C gradient in the system. We also want to know whether such a thermal gradient affects overall performance.

Other authors have measured the temperature dependence of APDs coupled to scintillation crystals for PET applications. For example, [13] observed a decreasing signal amplitude as a function of increasing temperature. A similar observation was made by [14]. Overall, the need for thermal regulation with APD based systems is clear. The study presented here goes beyond results presented in the aforementioned papers, since we are varying temperature and bias voltage simultaneously, and the studies were performed with a novel 3-D position sensitive PET detector. We want to predict an optimal bias voltage at each temperature. We also try to explain our results based on APD physical properties found in literature. The APDs used in this work are of a different type (see section 1.1.2) and have an area about 2 orders of magnitude larger than the APDs used by [13] and [14].

Although the focus of this work was applied to readout of PSAPDs, which other researchers such as [15–18] have incorporated into their PET system designs, the basic approach of study as well as the concepts of how to optimize bias voltage as a function of temperature and device gain would be helpful to those using APD arrays as well as PS-SiPMs [19] or SiPM arrays.

First, we will discuss some general properties of APDs, followed by a discussion of their temperature dependence. The second section describes experimental methods used in the paper. Section 3 presents the results of our measurements: first, we show the bias voltage dependence of leakage current, energy and time resolution and flood histogram accuracy at fixed temperature. Next, we present these performance parameters as a function of temperature and bias voltage. Finally, we propose different methods to predict the optimal bias voltage at different temperatures and we evaluate the performance of these methods. A discussion in section 4 provides interpretation of the observed behavior. Conclusions are summarized in section 5.

1.1 Properties of avalanche photodiodes

In avalanche photodiodes, the electron-hole pairs created upon impact ionization by the photoelectron gain so much energy from an externally applied electric field that these secondary carriers themselves become ionizing. An avalanche is thus established. In silicon, the average energy to create such an electron-hole pair, e_i, is 3.6 eV, despite the band gap of 1.1 eV. Scattering with phonons and with other charge carriers are also important energy loss mechanisms. Phonons describe the vibration of the lattice and are divided into two categories: acoustic and optical. The former have

2012 JINST 7 P08001

a longer wavelength than the latter. Optical phonon scattering is an important mechanism through which charge carriers lose energy. At 300K, the mean free path for phonon scatter λ_r is 38 Å for electrons and 62 Å for holes [20]. Typical APDs are about 250–300 μm thick, which is about 5 orders of magnitude larger than the mean free path for phonon scatter.

Other energy loss mechanisms such as carrier-carrier scatter, charge trapping and recombination at impurity centers can be important as well. A good review on charge transport can be found in [21].

Important parameters for the description of the avalanche process are the electron and hole ionization rate per unit traveled, $\alpha(x)$ and $\beta(x)$ respectively, which are position dependent. Using these, the gain $M(x)$ at a position x in the device can be expressed as: [22]

$$M(x) = \frac{e^{-\left(\int_x^w (\alpha(x')-\beta(x'))\mathrm{d}x'\right)}}{1-\int_0^w \alpha(x') e^{-\left(\int_{x'}^w (\alpha(x'')-\beta(x''))\mathrm{d}x''\right)}\mathrm{d}x'}, \tag{1.1}$$

with w the width of the avalanche region. Note that the denominator may become 0, yielding an infinite gain, corresponding to APD breakdown.

1.1.1 APD gain

The spatial dependence of the rates $\alpha(x)$ and $\beta(x)$ in equation (1.1) is due to a varying electrical field E as a function of depth x. It is illustrative to investigate how these rates change as a function of field strength E.

Based on a model developed by Baraff [23], Thornber [24] suggested an expression for $\alpha(E)$ valid at all fields:

$$\alpha(E) = \left(\frac{qE}{\varepsilon_i}\right) e^{-\frac{E_i}{E\left(1+\frac{E}{E_r}\right)+E_{kT}}}, \tag{1.2}$$

with E_i ($\mathcal{O}(10^6)\frac{\mathrm{V}}{\mathrm{cm}}$), E_r ($\mathcal{O}(10^5)\frac{\mathrm{V}}{\mathrm{cm}}$), and E_{kT} ($\mathcal{O}(10^4)\frac{\mathrm{V}}{\mathrm{cm}}$) the fields required for carriers to overcome decelerating effects of ionization, optical-phonon, and thermal scattering respectively. q is the elementary charge, ε_i is the high-field effective ionization threshold energy (3.6 (5.0) eV for electrons (holes) in silicon). The expression reduces to an $e^{-\frac{1}{E}}$ dependence for $E_{kT} < E < E_r$ and an $e^{-\frac{1}{E^2}}$ dependence for $E_r < E$, in agreement with an earlier expression found by Shockley [25] and Wolff [26] respectively. The $e^{-\frac{1}{E}}$ dependence of the ionization rate is often referred to as Chynoweth's Law: $\alpha = \alpha_\infty \cdot e^{-\frac{1}{E}}$ [27].

Many measurements of impact ionization in silicon [28–32] at intermediate fields led to various expressions for parameters a_∞ and b in Chynoweth's law. [33] argues that the reason for the discrepancies is a strong correlation between a_∞ and b when these are measured experimentally.

It is worth noting that the assumption that α and β are functions of E only is only valid in strong fields. In thin devices, nonlocal effects become significant, and history-dependent ionization coefficients need to be defined [34].

If we neglect the field dependence of α and β altogether, equation (1.1) can readily be integrated yielding:

$$M = \frac{(1-k)\, e^{(1-k)\alpha L}}{1-k e^{(1-k)\alpha L}}, \tag{1.3}$$

with L the length of the region where avalanche multiplication occurs and $k = \frac{\beta}{\alpha}$. We thus have approximated α by a rectangular function of width L. The ratio k is field dependent. In silicon β is

2012 JINST 7 P08001

about 2 orders of magnitude smaller than α at fields of about 200 kV/cm [28, 29, 31]. Expanding equation (1.3) around $k = 0$ we obtain:

$$M \overset{k\to 0}{\approx} e^{\alpha L}\left(1 + k\left(e^{\alpha L} - \alpha L - 1\right)\right). \tag{1.4}$$

Although greatly simplified, the above expression allows for a qualitative interpretation of device performance that we will use in this paper. Note that the expression between parentheses is always positive.

Due to the statistical nature of the avalanche process, an extra noise factor F is needed to describe the noise in avalanche photodiodes. F is referred to as excess noise which in the case of electron injection alone, is given by [22]:

$$F = kM + \left(2 - \frac{1}{M}\right)(1-k), \tag{1.5}$$

where $k = \frac{\beta}{\alpha}$ as before. In nonuniform electric fields k should be replaced by k_{eff} [35]:

$$k_{\text{eff}} = \frac{\int_0^w \beta(x) M^2(x) dx}{\int_0^w \alpha(x) M^2(x) dx}.$$

Note that the excess noise factor is small for small k.

If as depicted in figure 1 the APD is connected to an amplifier with one integrating and one differentiating stage with shaping time τ, the equivalent noise charge (the charge leading to a signal-to-noise ratio of one) is: [36, 37]

$$\text{ENC}^2 = \frac{1}{4}\left(\left(2qI_bF + \frac{1}{M^2}\left(2q(I_s + I_g) + \frac{4k_BT}{R_p}\right)\right)\tau + \frac{4k_BTR_sC_d^2 + e_n^2C_T^2}{M^2}\frac{1}{\tau}\right), \tag{1.6}$$

where I_b, I_s and I_g are the bulk, surface, and gate current in the preamplifier respectively. R_p the parallel resistance due to the APD, load resistance and preamplifier feedback resistance. R_s is the series resistance, C_d is the detector capacitance, e_n the noise voltage of the preamplifier, and C_t the total capacitance (the parallel combination of APD, stray and FET capacitance). k_B is the Boltzmann constant, and T the temperature. The expression does not take $1/f$ noise into account. The different contributions to the noise equation are shown in figure 1. From equation (1.6) it follows that for high gain devices, the main noise contribution is the bulk leakage current and the excess noise factor. Additional gain fluctuations due to spatial non-uniformities across the device may further degrade the noise performance.

1.1.2 APD devices

A multitude of different APDs have been designed, optimized for specific applications. In scintillation detection, three types of APDs are commonly used: 'reach-through' APDs, buried-junction 'reverse' APDs, and diffused junction 'beveled edge' APDs. Cross sections of these devices are shown in figure 2 and a brief summary of their performance is given in table 1.

Reach trough APDs, produced since the 1960s, are by far most commonly used in scintillation applications such as PET [36, 40, 41]. These devices feature a relatively thin multiplication region (1–10 μm) that has a large electric field ($\mathcal{O}(10^6)\ \frac{\text{V}}{\text{cm}}$). Photoelectrons need to transverse a large drift

2012 JINST 7 P08001

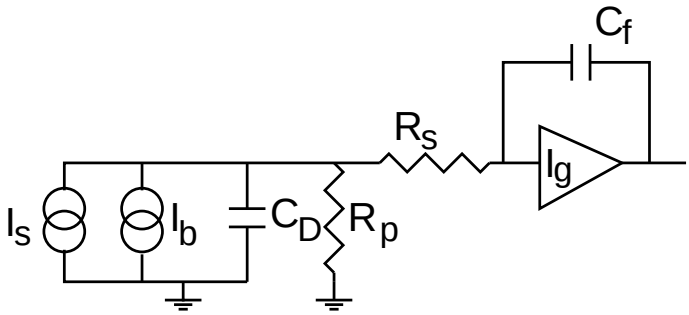

Figure 1. Equivalent circuit diagram of an APD coupled to a charge sensitive preamplifier. Currents, capacitors and resistors contributing to the ENC are indicated in the figure.

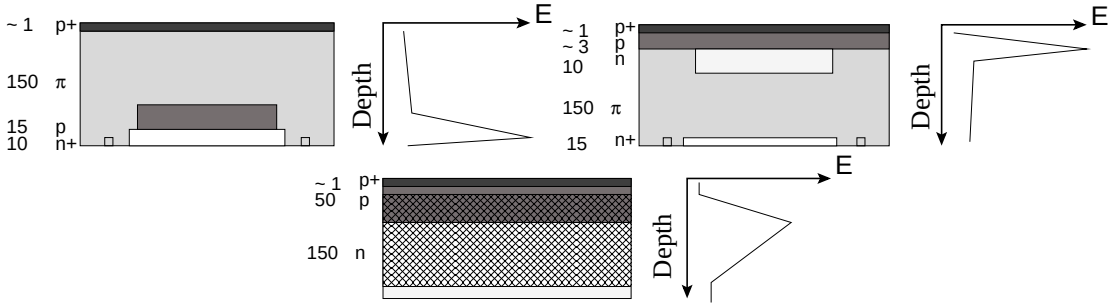

Figure 2. Cross section and electric field profile of various APDs. Upper left shows a 'reach-through' APD; upper right, a 'buried-junction'; lower center, a 'diffused junction' APD. The numbers on the left give the thicknesses of the various layers in μm.

Table 1. Qualitative properties of different types of APDs. Values are approximate. ([1] : [38], [2] : [39]).

type	drift region (μm)	multiplication region (μm)	gain	bias voltage	k_{eff} 10^{-2}
reach-through	100-150	1-10	100	100	1-5
buried junction[1]	< 10	1-10	< 250	400	0.700
diffused junction[2]	20	100	2000	1800	0.072

region (about 100–150 μm) before these are amplified. Buried junction APDs [42, 43] resolve the problems related to the large drift region by having the amplification region 'buried' about 10 μm below the surface. In contrast, diffused junction APDs have a relatively wide multiplication region (about 100 μm) in combination with a slightly smaller electric field (about 10^5 $\frac{V}{cm}$). These were initially referred to as 'beveled edge' APDs [44–46], because of the physical bevel present to prevent HV arcing across the device. These type of APDs have been characterized for radiation detection for example in [47]. A new production process [48] allowed construction of these diffused junction APDs without the need for physical bevel formation, thus allowing for a smaller dead area.

2012 JINST 7 P08001

[49] compared the behavior of reach-through and beveled edge APDs and concluded that the latter had a lower excess noise factor (due to the high gain and low k, see equation (1.5)) and a lower dark current, and thus a higher signal to noise ratio. The former had a lower operating voltage and faster speed of response. The high bias voltage of diffused junction APDs is often a disadvantage. It is worth noting that [50] describes a diffused junction APD with significant lower bias voltage (around 500 V instead of around 1800 V).

The devices used in this study are made by Radiation Monitoring Devices, Inc. (RMD). The junction is located about 60 μm below the surface. The depletion layer width w is about 150 μm at full bias voltage [51]. w varies as function of bias voltage as [35]:

$$w = \sqrt{\frac{2\varepsilon_s}{qN_B}\left(V_B - \frac{2kT}{q}\right)}, \tag{1.7}$$

with ε_S the silicon permittivity, q the elementary charge, N_B the majority carrier concentration (about $1.5 \cdot 10^{14}$ in our case), V_B the bias voltage, k the Boltzmann constant and T the absolute temperature. The multiplication region is about 90 μm wide [39]. The overall device thickness is 220 μm, including a SiO_2 passivation layer. The material used is 30 $\Omega \cdot$ cm n-type silicon. Maximum field strength of around 200 kV/cm at the junction can be expected. A $k_{\text{eff}} = 7.2 \cdot 10^{-4}$ has been measured [39]. Breakdown voltage is around $-1800V$.

1.1.3 APDs and scintillators

When used in combination with scintillators for PET, such as LSO in our case, the noise equation (1.6) needs to be updated to include the noise of the scintillator. If scintillator, APD and amplifier noise are quasi-Gaussian, the energy resolution can be written as [52]:

$$\left(\frac{\Delta E}{E}\right)_{\text{FWHM}} = 2.355\sqrt{\left(\frac{\text{ENC}}{N}\right)^2 + \frac{F-1}{N} + \frac{\alpha^2}{N}}, \tag{1.8}$$

where N is the effective number of photoelectrons generated, and ENC is the equivalent noise charge given by equation (1.6). The parameter α is the variance of the scintillator photons. Many authors have evaluated various scintillator-APD combinations, for instance [53, 54]. It is important to note that in the case of LSO α is quite large. [55] estimates the intrinsic energy resolution of LSO to be around 6 % at 662 keV. [56] measured an intrinsic resolution of 7.4 ± 0.5 % at 662 keV and 8.9 ± 0.6 % at 511 keV.

Another important parameter for PET instrumentation, is time resolution which is dependent on the scintillator decay time, the rise time of the signal, and the noise of the signal. For standard time-pickoff, the single detector time resolution is given by [57]:

$$\Delta t_{\text{FWHM}} = \frac{\sigma_V}{\mathrm{d}V/\mathrm{d}t}. \tag{1.9}$$

When using a constant fraction discriminator (CFD) for time pickoff, the exact expression of time resolution is complicated and beyond the scope of this paper. Equation (1.9) is sufficient for qualitative interpretation of the results presented here. A more elaborate expression can be found in [58].

2012 JINST 7 P08001

1.1.4 Effects of temperature on PSAPD performance

In section 1.1, we have omitted explicit temperature dependence of APD gain. It is clear that charge transport will be affected by temperature, due to different densities of states at different temperatures as given by the Boltzmann equation. According to [59], the band gap changes as a function of temperature chiefly due to temperature dependent electron-lattice interactions which cause a shift between valence and conduction bands:

$$E_g(T) = E_g(0) - \alpha \frac{T^2}{T+\beta}, \tag{1.10}$$

with $E_g(0) = 1.17$ eV, the band gap at 0 K, $\alpha = 4.73 \cdot 10^{-4}$ and $\beta = 636$ K [60] for silicon. Equation (1.10) is known as the Varshni equation. Measurements of the temperature dependence of the average energy needed to form an electron-hole pair in silicon, e_i, yielded the following expression: [61]

$$e_i(T) = 2.15 E_g(T) + 1.21, \tag{1.11}$$

a dependence that was also found in the calculations of [62].

APD gain (equation (1.1)) will be affected by temperature through the ionization coefficients $\alpha(x,T)$ and $\beta(x,T)$. Even today, an often cited model of temperature variation of the ionization coefficient is the one by [20]. Two of the three parameters in the model, the mean free path λ and the average energy per optical phonon scattering $\langle e_r \rangle$, have a temperature dependence given by:

$$\frac{\langle \varepsilon_r \rangle}{\varepsilon_r} = \tanh \frac{\varepsilon_r}{2k_B T} = \frac{\lambda}{\lambda_0}, \tag{1.12}$$

where $e_r = 0.063 eV$ is the optical phonon energy, k_B the Boltzmann constant and λ_0 the high-energy, low temperature asymptotic value of the phonon mean free path ($\lambda_0 = 47$ Å for electrons, and $\lambda_0 = 76$ Å for holes). The authors ignored the temperature dependence of the third parameter, e_i. A qualitative picture is that at lower temperatures, the mean free path increases, so electrons lose less energy to phonons and thus create more impact ionization, leading to enhanced charge multiplication. Experimental data by [28] at $T = 100$ K, 213 K, and 300 K, for fields between 200 and 400 kV/cm were well described by the model. Data obtained by [63] based on the breakdown voltage of avalanche photodiodes between 280 K and 580 K were also well described by a slightly modified version of this model for fields between 200 and 500 kV/cm.

Other authors have derived empirical expressions for Chynoweth's formula:

$$\alpha(T,E) = a(T) \cdot e^{\frac{-b(T)}{E}}. \tag{1.13}$$

[64] predicted that both $\frac{1}{b(T)}\frac{db}{dT}$ and $\frac{1}{a(T)}\frac{da}{dT}$ are constant. [31] described his 22−150°C data at fields varying between 200 - 500 kV using $b(T) = b_0 + b_1 \cdot T$, and $a(T)$ constant. The results of [33] at temperatures between 10°C and 160°C and fields 50 - 500 kV/cm were described by a similar expression. [65] also kept a constant, and $b(T) = b0 + b1 \cdot T$, based on a Monte Carlo calculation of impact ionization at different temperatures. [66] on the other hand used $a(T) = a_0 + a_1 \cdot T^2$ and $b(T) = b_0 + b_1 \cdot T$ for a theory developed for MOS device modeling at low temperatures.

[67] used a quadratic field dependence (E^2 instead of E in equation (1.13)), in combination with $a(T) = a_0 + a_1 \cdot T$ and $b(T) = (b_0 + b_1 \cdot T)^2$ to describe the temperature dependent ionization coefficient.

2012 JINST 7 P08001

Finally, [68] altered equation (1.13) to describe impact ionization up to very high temperatures (773 K):

$$\alpha(T,E) = \frac{E}{a(T) + b(T) \cdot e^{\frac{d(T)}{c(T)+E}}}, \tag{1.14}$$

with $c(T)$ and $d(T)$ quadratic and linear functions of T respectively. Chynoweth's law is recovered at room temperature and high field E. The functions $c(T)$ and $d(T)$ are needed to describe the behavior at high T and low field E.

The models of [20] and [67] fail to describe the ionization coefficient at low fields (below 100 kV/cm). At these lower fields, some of the assumptions used to develop their model are no longer valid.

The amount of leakage current also is an important temperature dependent observable of APDs. At lower temperatures, the leakage current decreases, due to fewer thermally generated electron-hole pairs. From equation (1.6), it follows that performance improves at lower temperatures.

Charge collection itself is dependent on the velocity of charge carriers in silicon, especially in not fully-depleted devices. When describing the velocity as a function of electric field E, two distinct regions are identified: a drift region and a saturation region. In the drift region, the speed of the carriers is proportional to the electric field. In the saturation region, the velocity reaches a limiting value $v_s(T)$ which does not increase with increasing field [69]:

$$v_s(T) = \frac{2.4 \cdot 10^7}{1 + 0.8 e^{\frac{T}{600}}} \quad (\mathrm{cm/s})$$

Drift and saturation velocity were studied by [69, 70]. The field at which $v_d(E,T)$ reaches $v_s(T)$ is temperature dependent.

Finally, the light output of LSO is temperature dependent. [71] measured temperature dependent light output variations dependent on the Cerium concentration and its location in the lattice. Changes between ± 5 % and up to ± 25 % for temperatures between 280K and 320K were observed. [72] on the other hand, measured a constant light output below 310 K. Temperature dependence of LSO light output also depends on the aspect ratio and light collection efficiency due to attenuation and temperature dependent trapping.

2 Materials and methods

2.1 Dual module

The modules used in the breast camera under development consist of two 8×8 arrays of $0.915 \times 0.915 \times 1$ mm^3 LSO crystals. Each of these arrays is coupled to two distinct, large area (1×1cm^2) PSAPDs, which are both mounted on the same Kapton flex circuit. Histomount[1] was used as an optical coupling agent between the crystal and the PSAPD surface. To prevent moisture from leaking into the PSAPD, the flex circuit is encapsulated with a layer of liquid crystal polymer (LCP[2]). An aluminum nitride (AlN_3) frame provides mechanical strength to the dual LSO-PSAPD module as well as electrical isolation. Figure 3 shows one dual LSO-PSAPD module.

[1] National Diagnostics (East Yorkshire, U.K.).

[2] Made by Nippon Steel Company, Japan: http://www.nscc.co.jp/english/materials/index.html.

2012 JINST 7 P08001

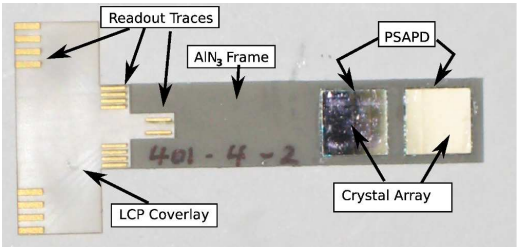

Figure 3. Top view of one of the dual LSO-PSAPD based detector modules used in the setup. The various parts are indicated in the figure. PSAPDs are located underneath the crystal arrays.

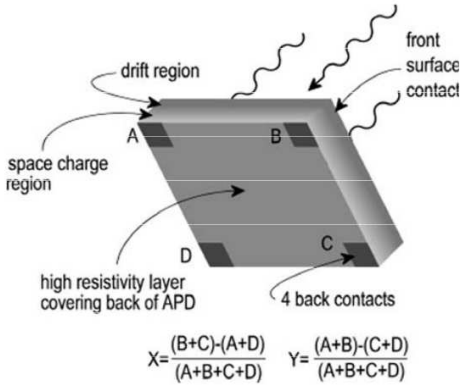

Figure 4. Schematic drawing of a PSAPD. Incoming radiation, front surface contact and 4 spatial channels are indicated in the figure. In this figure the X axis is a horizontal axis pointing to the right, the Y axis is pointing vertically up. Figure taken from [73].

The PSAPDs have 5 readout channels each, one on the front, for the $p-$side and four on the back, coupled to the $n-$side of the device across a resistive sheet giving spatial information [73]. The former is referred to as the *common* channel, the latter as *spatial* channels. Figure 4 shows a schematic drawing of the contacts on a PSAPD. The use of PSAPDs enables us to read out the 128 crystals in a dual LSO-PSAPD module using only 10 electronic channels. This number can be even further reduced by applying a dedicated multiplexing scheme [74]. From equation (1.6) we see that the additional series resistance is reduced by the gain M, and does not present a big contribution as long as the gain is large.

2.2 Electronics

Data in this paper were obtained using a ^{22}Na point source positioned in between a $0.9 \times 0.9 \times 1$ cm^3 lutetium-yttrium orthosilicate (LYSO) crystal coupled to a Hamamatsu H3164 photomultiplier tube (PMT) and a dual LSO-PSAPD module. For this report we collected and analyzed data from only one of the 8×8 LSO crystal array - PSAPD subunits in the dual module. Signals from the 4 spatial channels at the n-side, as well as the common p-side signal were connected to CREMAT CR-111 charge sensitive preamplifiers. These were housed on a custom made PCB which also held AC-coupling capacitors and bias resistors. The signal from the preamplifiers was fed into NIM based ORTEC-855 spectroscopy amplifiers, whose shaping time was set to 500 ns, the minimum value of these amplifiers. The shaping time is large compared to the decay time of LSO, which is about 40 ns.

2012 JINST 7 P08001

The signal from the common was used to extract timing information. We used a Fast Filter Amplifier with differentiation time of 20 ns and integration time 50 ns and an ORTEC 935 CFD. These integration and differentiation times were optimized for best timing performance. To eliminate time walk, the delay in the CFD was set to 94 ns. The threshold was adjusted depending on bias voltage and temperature so that at any temperature and voltage a similar trigger rate was obtained.

The PMT signal was split into a CFD with 9 ns delay and into a spectroscopy amplifier so that energy and time resolution from the reference PMT could be accurately measured.

The signals from both CFDs were fed into a time to amplitude (TAC) converter. A variable fine delay between the PMT and the TAC module allowed for calibration of the TAC module.

Two National Instruments PCI-6110 digitizer cards were used (8 total channels). The trigger was formed by a gate and delay generator module (ORTEC 416A) connected to the TAC. Delay amplifier modules (ORTEC 427A) were used to ensure that sampling occurred at maximum pulse amplitude.

In order to investigate the noise in the system in absence of a signal ($I_{sig} = 0$ in equation (1.6)), we connected a 2 V pulse across a 1 pF capacitor connected to the input of the common channel preamplifier. The amplitude of the observed pulse was 2 V. The combined gain of the readout electronics thus was 1 V per pC of injected charge for the common channel.

2.3 Gain calibration

According to [75], 28800 ± 1500 photons are created per MeV energy deposition in LSO. The quantum efficiency of the PSAPD is about 90 % at the emission wavelengths of LSO [51]. Using the DETECT2000 [76] simulation package, a light collection efficiency of 90 % was estimated. Multiplying these numbers together, we obtain an estimated gain of 539 ± 40 per Volt digitized by our electronics. Note that this is only an estimate as the exact light yield and the quantum efficiency are hard to measure experimentally. Nonetheless the calculated gain is a good approximation and gives an idea about the order of magnitude of the gain.

2.4 Leakage current

The leakage current was measured on an event-by-event basis by reading out the voltage drop across a bias resistor. This potential difference was buffered, amplified and finally digitized by a National Instruments PCI-6143 ADC, which was triggered by the signal from the gate generator. After gain calibration and using Ohm's law, the leakage current could be measured. The currents from each of the two PSAPDs in a module were digitized separately. The sum of these two leakage current values agreed to within 15 % of the value given by the HV power supply. Leakage current typically ranged from 0.5 to 2.5 μA depending on bias voltage (around 1720 V) and temperature.

2.5 Temperature control

The entire setup was placed in an airtight dark box. In order to prevent condensation at low temperatures, the box was flushed with dry air during data acquisition. A relative humidity of about 10 % was reached.

A thermo-electric (Peltier) element was attached to the back side of the module using thermal paste. The hot side of the Peltier element was connected to a copper heatsink which had a radiator attached to it. A fan blew air across the cooling fins to cool the heatsink.

2012 JINST 7 P08001

Temperature was measured via a K-type thermocouple glued to the module. Due to the thermal conductivity of aluminum nitride (175 $\frac{W}{m \cdot K}$), it is safe to assume that the PSAPDs were at the same temperature as measured by the thermocouple. The temperature was kept constant within 0.1 °C by carefully adjusting the current to the Peltier element and monitoring the thermocouple readings. More details are found in [77].

2.6 Analysis

In order to determine spatial coordinates, the signals from the four corners of the resistive sheet A, B, C and D were combined using 'Anger'-type logic as follows:

$$\begin{aligned} x &= \frac{(A+B)-(C+D)}{A+B+C+D} \\ y &= \frac{(B+C)-(A+D)}{A+B+C+D} \end{aligned} \tag{2.1}$$

The data were further analyzed using in house code developed based on the ROOT package [78]. An algorithm localized all 64 peaks in the flood histogram automatically. Next, these 64 peak locations were ordered in a logical way. Incoming photon events were assigned crystal locations based on the minimum distance to the nearest peak. Next, a sum of a constant, an exponential and a Gaussian function was fit to all 64 crystal energy spectrum histograms. In order to improve the accuracy of energy resolution determination, the spectra of the individual crystal elements were combined into a global spectrum after correcting for variations in PSAPD gain and relative light yield differences between crystal elements. For timing analysis, only events that fell within $^{+4}_{-3}\sigma$ of the photopeak energy of every individual crystal were used. To obtain time resolution for all 64 crystals, a Gaussian was fit to the TAC histogram for every individual crystal.

The flood histogram itself was described by a figure-of-merit (FOM) for each row, which compares the distance between individual crystal peak positions and the width of their distributions. Due to non-linear charge sharing [79] and reduced gain at the edges of the PSAPD, the outer two rows were excluded from the FOM calculation, since the measured position of crystals in these rows are systematically closer to each other and their width is systematically larger, thus introducing a systematic bias. The FOM for inner row j was obtained as:

$$\mathrm{FOM^j} = \frac{\frac{1}{5}\sum_{i=2}^{6} X_{i+1}^{j} - X_i^{j}}{\frac{1}{6}\sum_{i=1}^{6} \sigma_i^{j,X}}, \tag{2.2}$$

with X_i the x position of peak i and σ_i^X its width in the x direction. A larger FOM indicates superior performance. The FOM can be defined both in the X and Y direction. Due to symmetry we analyzed the FOM only in the X direction.

3 Results

3.1 Fixed voltage and temperature measurements

As a reference, we present data at 17°C and a bias voltage of 1725 V in figure 5. The rightmost panel shows a flood histogram. All 64 crystals are clearly identifiable in the figure. The upper left

2012 JINST 7 P08001

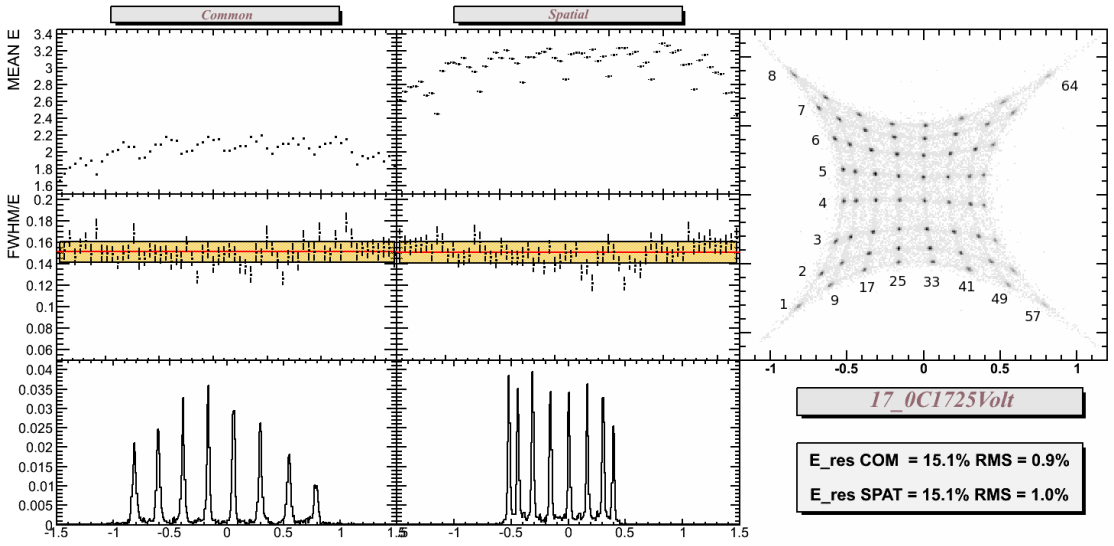

Figure 5. Upper left and middle show the photopeak position for every crystal of the array for common and spatial channels respectively. Center left and middle panel show the energy resolution of every crystal. The band represents mean ± 1 RMS. Lower left and center show a profile through the top and center rows of the flood histogram shown in the right panel of the figure.

and upper central panel show the photopeak position for every individual crystal for the common and spatial channels respectively. The photopeak position takes both PSAPD gain and light yield of each individual crystal into account. As expected, the gain follows a similar pattern for common and spatial channels. The overall gain difference between common and spatial channels is due to different settings of the NIM amplifiers.

The center left and middle panel of the figure show the energy resolution (photopeak FWHM/mean) for common and spatial channels, respectively, for every individual crystal of the array. An average FWHM energy resolution of 15.1 ± 0.9 % (RMS) for spatial channels and 15.1 ± 1.0 % (RMS) for the common was observed at 511 keV.

The lower left and lower central panel show a profile through a top and center row of the flood histogram respectively. Peaks in the profile histogram correspond to events attributed to individual crystal pixels. All peaks are normalized to one. We see that at the top row, the peaks are broader, but also more spread out. In the center row, the peaks have the same width. From these figures it is also clear that due to edge effects, the profiles are systematically different for the outer crystals compared to the ones in the center.

In order to account for PSAPD gain variation and light yield effects from the different crystals in the array, and to improve statistics, the energy spectra from individual crystals were combined after scaling with a factor $\frac{\bar{g}}{g_i}$, where g_i is the gain of crystal i and $\bar{g}$ the average gain of all crystals. The resulting energy histogram is shown in figure 6. The photopeak is clearly visible. The left hand side of the photopeak shows a broadening due to $X-$ray escape from these miniscule crystal elements, as also observed in [8]. A Gaussian plus constant background were fitted to the right hand side of the spectrum:

$$f = p0 + p1 \cdot e^{-\frac{1}{2}\left(\frac{x-p2}{p3}\right)^2}. \tag{3.1}$$

2012 JINST 7 P08001

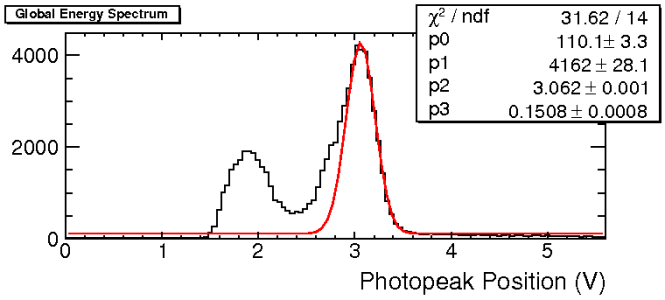

Figure 6. Global energy spectrum (after calibrating for individual crystal variations) for spatial channels. The fit function of equation (3.1) was fit to each spectrum. Fit parameters are indicated in the figure.

The fit function and its parameters are shown in the figure. A gain-corrected global energy resolution of 11.57 ± 0.06 % and 10.94 ± 0.23 % FWHM at 511 keV were obtained for spatial and common energy resolution respectively. These values are lower than the ones shown in figure 5, because of the lack of a correction for X-ray escape in that figure. By fitting only the right hand side of the histogram in the global energy spectrum, the effects of $X-$ray escape are eliminated. The latter approach is only possible when sufficient statistics are available, and thus it cannot be applied to the energy spectra of the individual crystals.

3.2 Bias voltage dependence

The variation in energy resolution as function of bias voltage at constant temperature $T = 17°\mathrm{C}$ is depicted in figure 7. Between 1700 V and 1730 V, no significant improvement as a function of bias voltage can be seen. At higher voltages the energy resolution systematically degrades, which can be attributed to an increased excess noise factor and an increased leakage current yielding degraded energy resolution, as suggested by equations (1.6) and (1.8). We did not try to scan the entire bias voltage range in search of optimal gain because, as shown in the next paragraphs, both the flood histogram and time resolution require high gains.

The energy resolution insensitivity at lower bias voltages indicate that at these voltages, energy resolution is dominated by the LSO crystal (α in equation (1.8) is the dominating contribution). Similar behavior was observed elsewhere [80]. Also [81] measured a > 8 % energy resolution across a wide variety of LSO boules.

Figure 8 shows the average FWHM coincidence time resolution for the 511 keV photo peak. Coincidence time resolution improves as a function of bias voltage until it reaches a minimum plateau beyond which the time resolution deteriorates. The behavior can be explained by equation (1.9): $\frac{\mathrm{d}V}{\mathrm{d}t}$ decreases with increasing bias voltage due to an increased depletion layer as a function of high voltage. This causes the width of the drift region to decrease (the region between the depletion layer and the contacts) and hence leads to a shorter drift time. In addition, the expanding depletion layer also causes a decrease in device capacitance, thus shortening the RC-dependent rise time. The deterioration at higher voltages is due to increased noise in the signal σ_V, because of an increased excess noise factor. This increase in noise at higher bias voltage was also observed in the energy resolution plots (figure 7).

2012 JINST 7 P08001

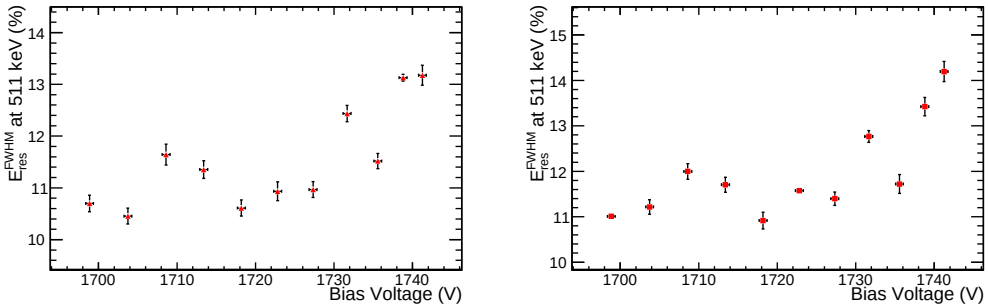

Figure 7. FWHM energy resolution at 511 keV as a function of bias voltage for the common (left) and spatial channels (right). Data obtained at 17.0°C.

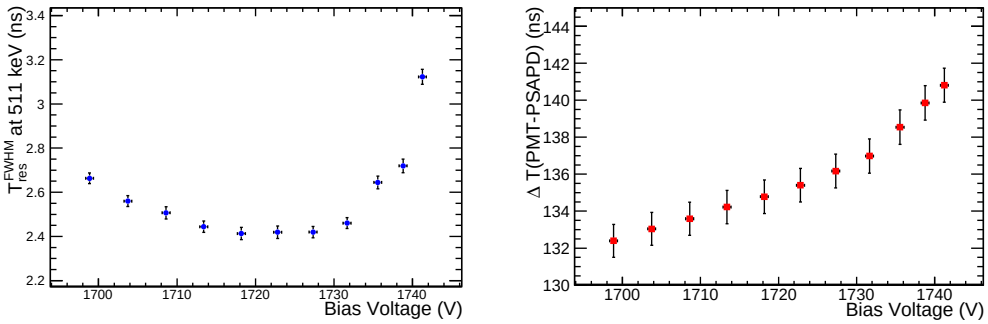

Figure 8. Average FWHM coincidence time resolution at 17.0°C over all crystal pixels as a function of bias voltage. A plateau of optimal bias voltage is observed (left). Right shows the mean difference in arrival time between the PMT and PSAPD signal as a function of bias voltage.

Figure 8 also shows the mean difference in arrival time between PMT and PSAPD as measured by the TAC. The time difference increases as a function of bias voltage, explained by a larger rise time for larger signals (which does not mean a smaller $\frac{dV}{dt}$). A CFD is only able to correct timing walk for signals with the same rise time. The error bars in the plot are large due to a spread of about 20 ns in arrival time depending on the crystal location, as also observed in [8] and [82]. Two distinct regions with different slopes are observed in the figure, we will discuss this transition in section 4.

The quality of the flood histogram expressed via FOM (equation (2.2)) as a function of bias voltage is shown in figure 9. Also here a plateau of superior performance is observed for both edge and center rows ($\mathrm{FOM_{Edge}} = \frac{1}{2}(\mathrm{FOM}^1 + \mathrm{FOM}^8)$ and $\mathrm{FOM_{Center}} = \frac{1}{2}(\mathrm{FOM}^4 + \mathrm{FOM}^5)$). The degradation at higher voltage can be attributed to a higher excess noise factor, increasing both shot noise due to the signal and shot noise due to the leakage current (equation (1.6)).

In order to better understand the FOM, it is illustrative to analyze both of its components: distance between peaks and width of the peaks. The distance between peaks is plotted in figure 10. Taking $(A-B)+(D-C) = f\cdot(A+B+C+D) = fI_{\mathrm{light}}$, equation (2.1) can be rewritten to include

2012 JINST 7 P08001

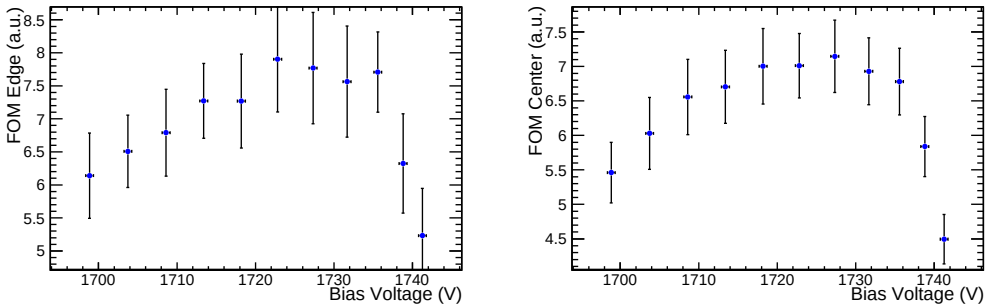

Figure 9. FOM for the top (left) and center (4th) (rights) rows as a function of bias voltage.

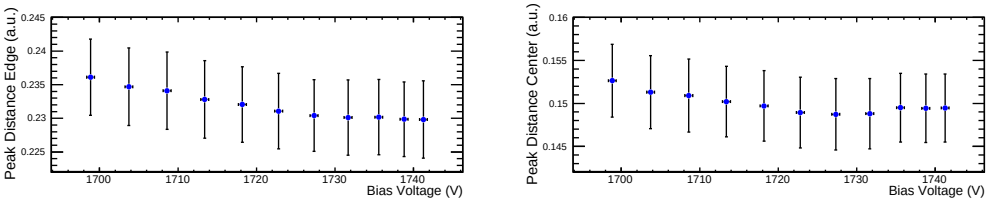

Figure 10. Distance between the central crystal location peaks in the flood histogram for the edge (left) and center (4th) (right) rows as a function of bias voltage.

noise sources due to the leakage current from the four corner signals $\delta_i (i = A,B,C,D)$:

$$x = \frac{f \cdot I_{\text{light}} + \delta_A - \delta_B + \delta_C - \delta_D}{I_{\text{light}} + \delta_A + \delta_B + \delta_C + \delta_D} \approx \frac{f \cdot I_{\text{light}}}{I_{\text{light}} + 4 \cdot \delta_A}, \tag{3.2}$$

where the approximation is based on the assumption that the non-proportional noise δ_i is the same in each quadrant, i.e. $\delta_A \approx \delta_B \approx \delta_C \approx \delta_D$. Due to AC-coupling, the mean of the leakage current contribution δ_i should be 0, however its width is not. Both the width of the I_{light} and δ_i distributions goes as $\sigma^2 = F(M) \cdot M^2 \Delta f$ (equation (1.6)). The exact calculation of the mean of x in equation (3.2) is beyond the scope of this paper. It suffices to say that the above expression yields a spatial compression of the flood, indicated by the data presented in figure 10. Above 1730V, no decrease in distance between crystal peaks is seen, due to a higher excess noise factor not taken into account in equation (3.2). Because of the decreased distance between peaks, the width of the peaks in the position histogram is a better observable than the FOM of figure 9 and this parameter will be used in the next section.

3.3 Combined temperature and bias voltage dependence

Figure 11 shows the variation of gain and leakage current as a function of bias voltage and temperature. Data was taken at 11 different temperatures. At lower temperatures the gain increases faster with bias voltage, an effect explained by equation (1.13) on page 7: taking $a(T) = a$ and $b(T) = b_0 + b_1 \cdot T$, the exponential increases if T decreases. The bias voltage at which the gain steeply rises is lower for lower temperatures, consistent with many predictions and observations in

2012 JINST 7 P08001

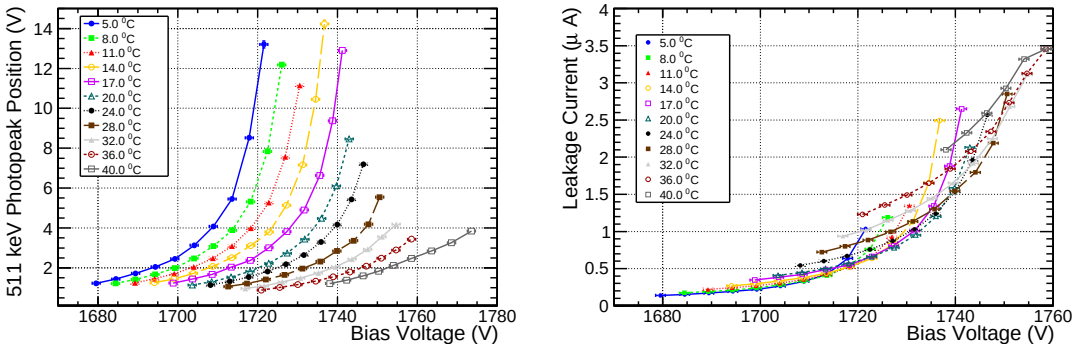

Figure 11. Left: Gain as expressed by the 511 keV photopeak position at various bias voltages and temperatures. The right panel shows the leakage current at different bias voltages and temperatures.

the literature showing that the breakdown voltage decreases as a function of temperature. The range of bias voltage measurements at any temperature varied depending on the observed leakage current and gain. At lower temperatures, a lower leakage current is observed due to the decrease in thermally generated electron-hole pairs. Leakage current increases with bias voltage, because the bulk leakage current is subject to avalanche multiplication. The fact that the leakage current decreases as the temperature decreases indicates that we were effectively cooling the module, without reaching the limits of our cooling setup. With the gain calibration of section 2.3, gains between roughly 540 (photopeak position at 1 V) and 4850 are observed (photopeak position at 9 V) in figure 11.

Gain as a function of temperature is shown in figure 12. Data points were obtained from an interpolation of the data presented in figure 11. The left panel shows that gain decreases as a function of temperature. Using the equation $V_B = \frac{E \cdot W}{2}$ [35], with V_B the bias voltage, E the electric field, and W the depletion layer width, and combining equation (1.13) and equation (1.3) we can write:

$$M = \frac{(1-k)\,e^{(1-k)\left(a_0 \cdot e^{-\frac{(b_0+b_1 T)W}{2V_b}}\right)L}}{1-ke^{(1-k)\left(a_0 \cdot e^{-\frac{(b_0+b_1 T)W}{2V_b}}\right)L}} = \frac{(1-p_3)\,e^{(1-p_3)\left(p_0 e^{-\frac{(p_1+p_2 T)W}{2V_b}}\right)}}{1-p_3 e^{(1-p_3)\left(p_0 e^{-\frac{(p_1+p_2 T)W}{2V_b}}\right)}}. \tag{3.3}$$

In order to reduce the number of fit parameters, W was estimated from equation (1.7) to be 125 μm, and the bias voltage dependence of $k = a_0$ was ignored. The function of equation (3.3) was fit to the data presented figure 12. The fitting procedure was underdetermined due to the relation between the fitting parameters, in particular parameters p_3 and p_0. Therefore good initial estimates were required for the fit. Nonetheless, we obtain a value of $p_3 = k = 1.42 \cdot 10^{-3}$, in good agreement with [39] who obtained $k = 0.7 \cdot 10^{-3}$ for a similar device. $p_1 = b_0 = 1.11 \cdot 10^6$ and $p_2 = b_1 = 1.4 \cdot 10^3$ agree well with $b_0 = 1.05 \cdot 10^6$ and $b_1 = 1.3 \cdot 10^3$ obtained by [31]. Estimating error bars on the fit parameters is challenging because of the cross correlation between the fit parameters and the limited data. The important observation here is that the order of magnitude of the fit parameters agrees well with values from literature and shows that we understand our experimental parameters.

2012 JINST 7 P08001

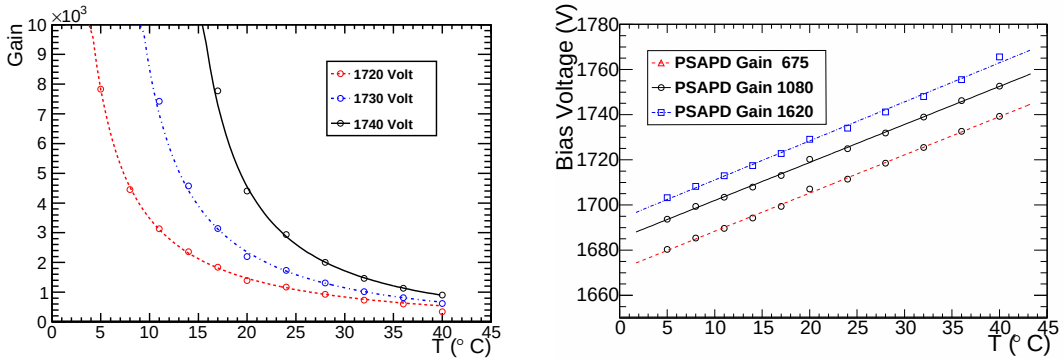

Figure 12. Left: gain variation as a function of temperature at three different bias voltages. The lines indicate the fit function of equation (3.3). The right figure shows the bias voltage required to maintain a fixed gain as a function of temperature, for three different photopeak positions. Gain is expressed as voltage at the ADC's input.

The right panel of figure 12 shows the bias voltage needed to obtain a fixed gain as a function of temperature, for three different gain values. At lower temperatures, lower bias voltages lead to the same device gain. Data was obtained by interpolating the values of figure 11. Fits to the curves yielded slopes of $1.69 \pm 0.02 \frac{V}{°C}$, $1.68 \pm 0.02 \frac{V}{°C}$ and $1.73 \pm 0.03 \frac{V}{°C}$ for gains corresponding to 1.25 V, 2.00 V, and 3.00 V respectively, in good agreement with each other, indicating a bias voltage temperature coefficient independent of the value of the gain.

Time resolution is strongly affected by temperature and bias voltages, as seen in figure 13. The time resolution degrades between 40°C and 20°C, but no improvement below 20°C is observed. The improved time resolution as a function of temperature can be explained by equation (1.9): $\frac{dV}{dt}$ increases at lower temperatures due to an increased drift velocity (see for example [63]). σ_V in equation (1.9) is also reduced because of the decreased bulk leakage current (see equation (1.6)) and decreased thermal noise from the resistive sheet connected to the PSAPD. The observed temperature independence below 20°C can be attributed to different effects: noise of the scintillator, time resolution of the LYSO-PMT used in coincidence with the LSO-PSAPD module, and the noise of the electronics.

To exclude influence of the PMT, we can analyze the quality of the flood histogram through the FWHM of the peaks, shown in figure 14. A similar pattern as the one observed in figure 13 is obtained. Overall performance is better at low temperature, and is bias voltage dependent. A limited improvement can be seen for temperatures below 17°C degrees. The improvement in peak width as a function of temperature is attributed to a decrease in noise caused by a decreased leakage current. Such an improvement was also observed by [16]. As opposed to figure 13, a small yet noticeable improvement below 20°C is observed, indicating that PMT time resolution plays a role in the overall coincidence time resolution in figure 13.

3.4 Optimal bias voltage prediction

For systems comprising many semiconductor detectors, a method to relatively quickly determine the optimal operating bias voltage is desirable. Data presented in the previous sections suggest

2012 JINST 7 P08001

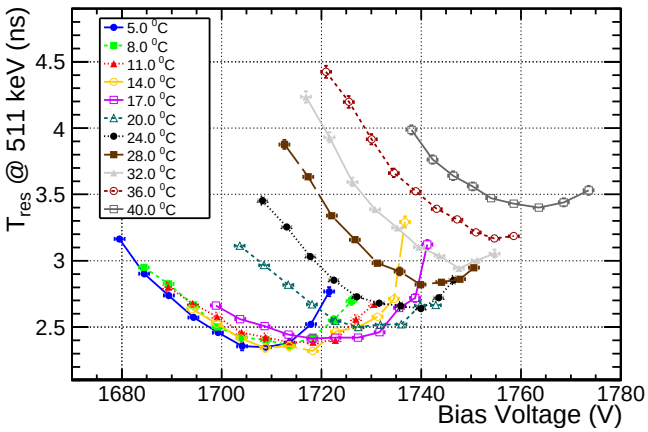

Figure 13. FWHM Coincidence time resolution at 511 keV at different temperatures as a function of bias voltage.

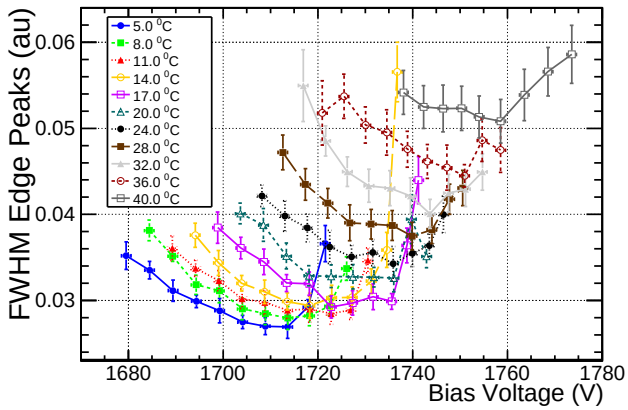

Figure 14. Average FWHM of the crystal peaks seen in the flood histogram as a function of bias voltage at different temperatures.

an optimal bias voltage that maximizes time resolution and improves the quality of the flood histogram which is different at different temperatures. This section presents a method of predicting that optimal bias voltage. Two methods are proposed: one based on the time resolution, and one based on an intersection method.

3.4.1 Time resolution method

Time resolution may be a good observable for predicting the optimal bias voltage. In order to perform this optimization, a third order polynomial was fit to the coincidence time resolution versus bias voltage for every temperature as displayed in figure 13. We hypothesize that the minimum of the third order polynomial corresponds to the optimal bias voltage at that temperature. The energy resolution, time resolution and FOM data were interpolated at this optimal bias voltage for every

2012 JINST 7 P08001

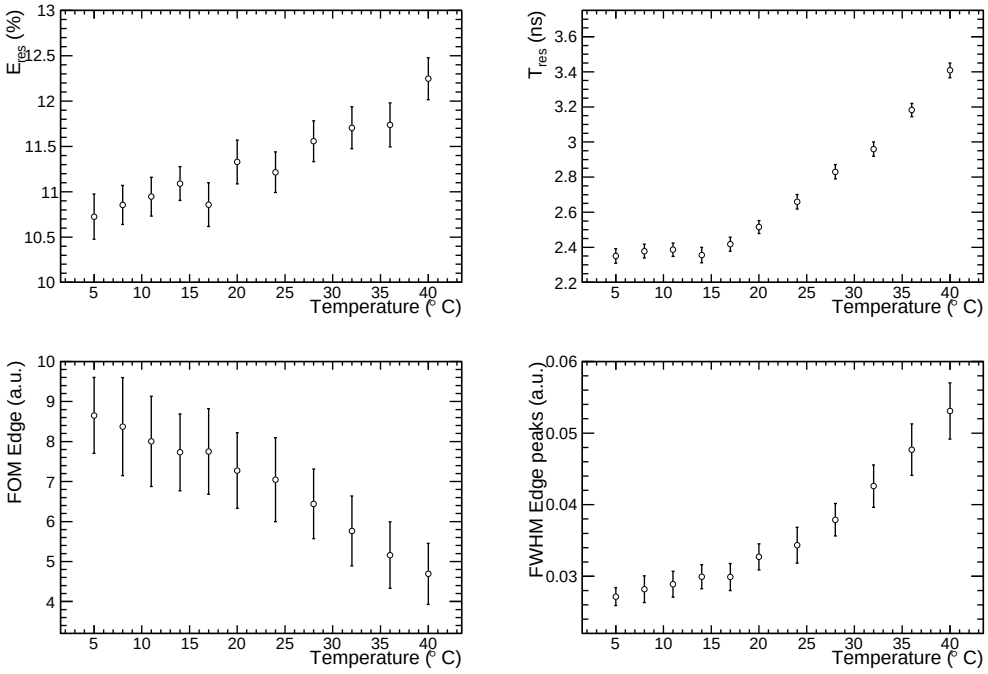

Figure 15. Energy resolution for the common channel (upper left), coincident time resolution (upper right), FOM at the edge row (lower left) and width of the peaks in the top row of the flood histogram (lower right) at the optimal bias voltage predicted by the third order polynomial fit to the time resolution versus temperature curve.

temperature, yielding a performance measure of various parameters versus temperature at optimal bias voltage which is shown in figure 15. We see that all observables improve with decreasing temperature. A linear fit to the energy resolution showed a degradation of $0.038 \pm 0.006\ \frac{\%}{^\circ C}$ between 5°C and 40°C. Above 15 degrees coincidence time resolution deteriorates by $0.042 \pm 0.002\ \frac{\text{ns}}{^\circ C}$, and the FOM decreases by $0.11 \pm 0.02\ \frac{1}{^\circ C}$. The width of the peaks in the flood histogram show a quadratic dependence on temperature. As also observed from figure 13, the time resolution stays within 10 % of its optimal value over a range of 32 ± 5 V at any temperature between 5°C–40°C.

3.4.2 Intersection methods

Using the time resolution as an estimator for the optimal bias voltage is impractical, since it requires a time consuming coincidence setup and a radioactive source. Therefore we investigated other methods to predict the optimal bias voltage.

Figure 16 shows the photopeak positions (gain) for the spatial channels as a function of bias voltage at different temperatures. An exponential function was fit to the data points at lower bias voltage and another one was fit to data points at higher bias voltage. For temperatures lower than 24°C two distinct regions can be observed: one having a lower slope than the other. The increased slope at higher voltage is an indication of the onset of hole multiplication in the avalanche process: the change in gain is higher, because holes are also contributing to the overall gain above a certain bias voltage. We will come back to this topic in section 4.

2012 JINST 7 P08001

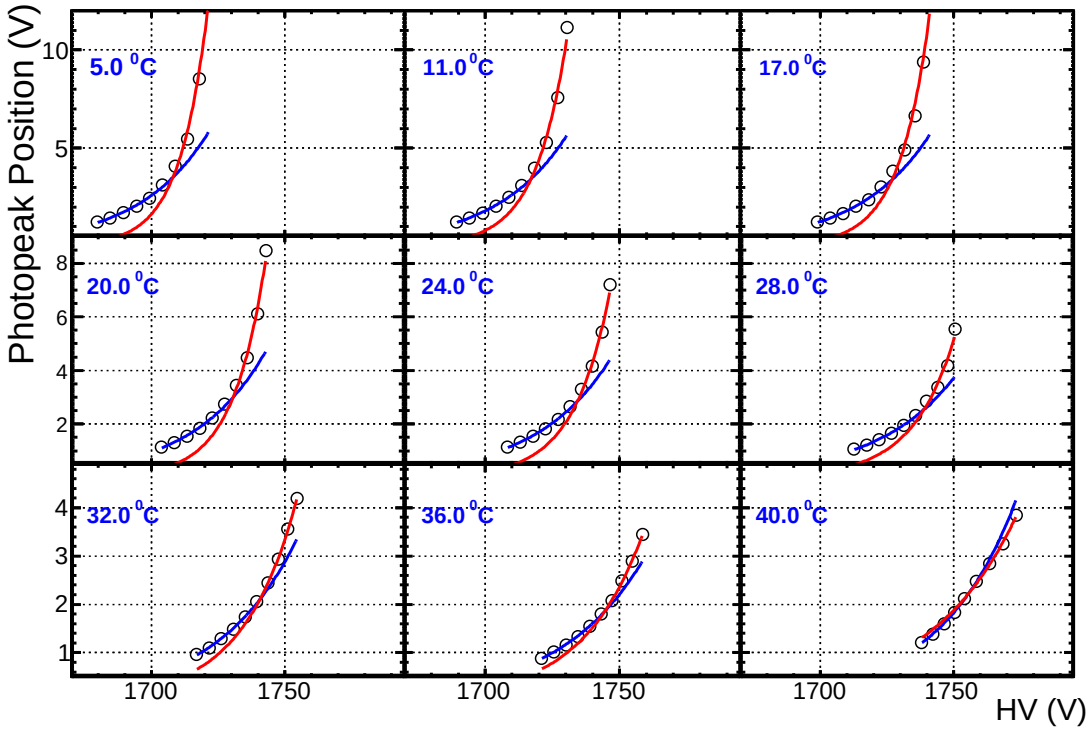

Figure 16. Photopeak position of the spatial channels for different temperatures as a function of bias voltage.

At higher temperatures the two exponentials overlap, and two distinct regions are not observed. At these temperatures the holes do not gain enough energy to start impact ionization due to interactions with the increased amount of thermally generated electron-hole pairs.

Similar dual-exponential behavior was observed for the photopeak position from the common channel as well as for the leakage current, confirming the suggestion that the effect is related to a device property. The slopes (b in $y = e^{a+bx}$) of the bi-exponential fit to spatial channels gain, common channel gain and leakage current are shown in figure 17. Good agreement between the slopes of spatial and common channel gain are observed for both lower and higher gain exponentials. The slope of the exponential fits to the leakage current follows a similar pattern. The slopes of the higher gain exponentials decrease as a function of temperature until they merge with the lower ones at high temperature. Interestingly the slopes of the lower gain exponential is only weakly dependent on temperature, explaining the behavior observed in the right panel of figure 12.

We will investigate if the bias voltage corresponding to the intersection of the two exponentials could be an indication of optimal bias voltage at each temperature. For voltages below the intersection point, time resolution is not optimal due to a decreased $\frac{dV}{dt}$. Voltages above the intersection have more noise, since the onset of hole multiplication causes a larger k and thus also a larger excess noise factor (equation (1.5)).

The bias voltages at which the intersection occurs are shown in figure 18. The intersections of the common and spatial channel gains as well as those based on the leakage current agree well.

2012 JINST 7 P08001

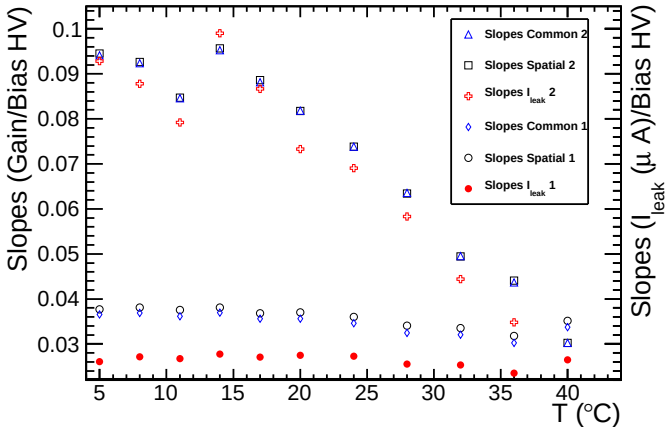

Figure 17. Slopes of exponential curves fitted to the photopeak position of the common and spatial channels, as well as to the leakage current data (for which the unit is displayed on the right in μA/V). At every temperature two exponentials were fit to the parameter (gain, leakage current) versus bias voltage curve.

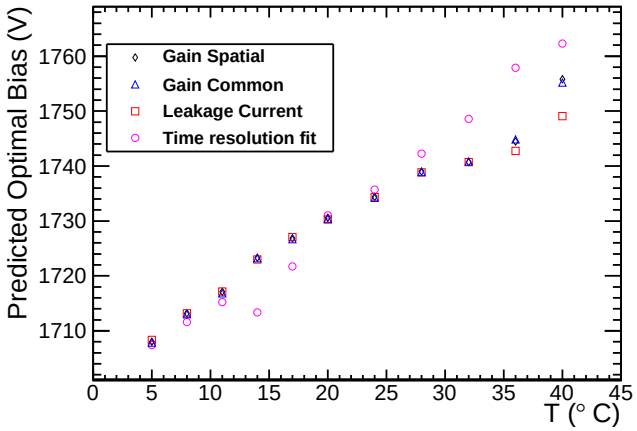

Figure 18. Bias voltage at which the two exponentials in figure 17 intersect. The points of intersection based on the gain of the common channel and the leakage current are also shown. In addition, the bias voltage corresponding to optimal time resolution is included.

The same figure also shows the optimal bias voltage predicted by the time resolution method. A relatively good agreement is observed, except at higher temperatures, where the intersection point is harder to predict due to similar slopes in the high and low gain regions. As expected, optimal performance is achieved at higher bias voltages for higher temperatures. A first order polynomial fit to the optimal bias voltage based on the time resolution data yields a slope of 1.64 ± 0.07 $\frac{V}{^\circ C}$. The point at 14°C seems to be an outlier. Due to the polynomial fit to the time resolution statistical fluctuations can be amplified.

2012 JINST 7 P08001

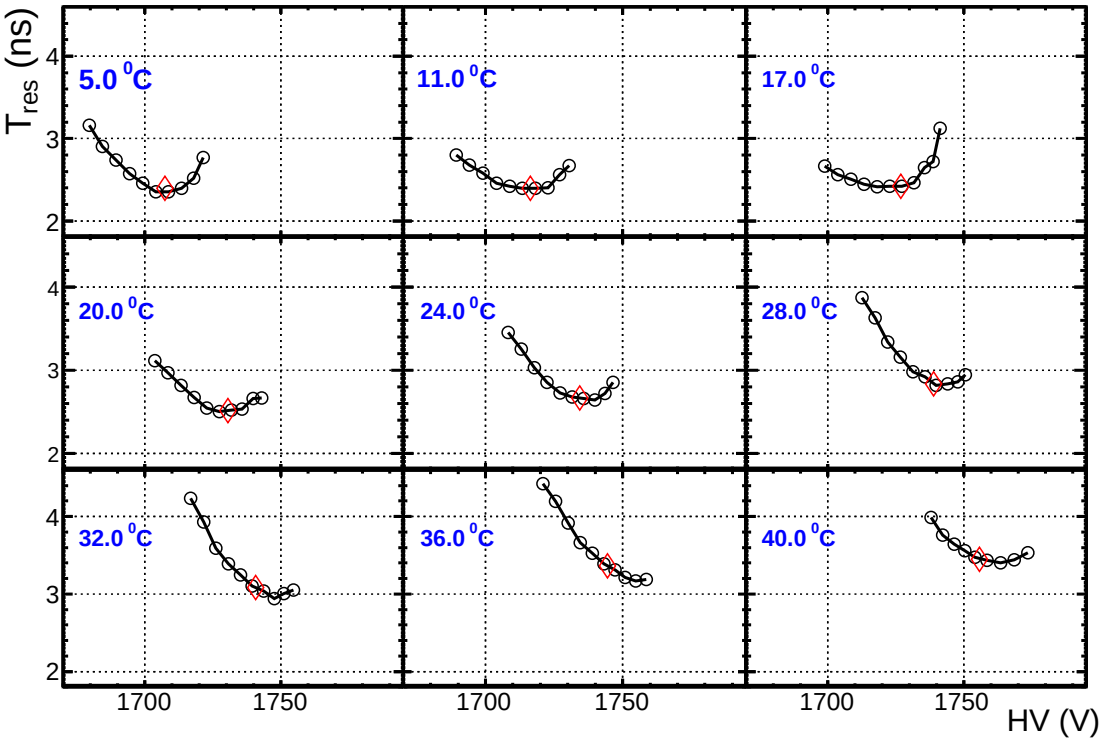

Figure 19. Time resolution at different temperatures. The diamonds indicates predictions of the optimal time resolution based on the intersection method.

To evaluate the performance of the intersection method, the predicted best coincidence time resolution at these optimal bias voltages is plotted on the time resolution curves of the full data set at various temperatures in figure 19. The time resolution at these predicted bias voltages are indicated by diamonds in the figure. Below 28°C, the diamond corresponds to the bias voltage at which the time resolution is minimum. At higher temperatures the agreement is worse, again due to a lack of distinction between low and high gain region.

Table 2 compares the optimal bias voltage and the gain, leakage current and time resolution as predicted by the time resolution method and the intersection method. Again, larger differences are observed for temperatures >28°C. Percentage differences (indicated in the table) for bias voltages and time resolution are low, but the differences in predicted gain and leakage current are substantial. These differences are attributed to the exponential rate of change, whereby a small difference in bias voltage (Δx) results in large changes in gain and leakage current (Δy). The optimal gain as given by the time resolution method is on average 1470 ± 140 (RMS). The optimal gain thus is relatively constant.

4 Discussion

The gain and leakage current data show two distinct regions as a function of bias voltage, one having a higher rate of change than the other. This larger increase in gain at higher voltages

2012 JINST 7 P08001

Table 2. Predicted optimal bias voltage and performance parameters at these voltages based on the intersection method (i) and the time resolution method (t). The intersection method uses leakage current data. Percentage differences in performance between the two methods are shown as well.

temperature	$bias_i$	$bias_t$	Δ	$Gain_i^c$	$Gain_t^c$	Δ	$I_{leak,i}$	$I_{leak,t}$	Δ	$t_{res,i}$	$t_{res,t}$	Δ
$^\circ C$	V	V	%			%	μA	μA	%	ns	ns	%
5	1708	1707	0.1	1467.88	1359.15	6.0	0.3	0.3	4.9	2.35	2.35	0.2
8	1713	1712	0.1	1359.15	1250.42	8.5	0.4	0.4	7.1	2.36	2.37	-0.5
11	1717	1715	0.1	1359.15	1196.05	12.6	0.5	0.5	10.2	2.4	2.4	0.1
14	1723	1713	0.6	1413.52	924.222	53.3	0.6	0.4	47.6	2.47	2.36	4.7
17	1727	1722	0.3	1359.15	1032.95	32.6	0.8	0.6	26.5	2.42	2.42	0.2
20	1730	1731	-0.0	1141.69	1196.05	-3.5	0.9	0.9	-3.0	2.51	2.52	-0.1
24	1734	1736	-0.1	1087.32	1196.05	-7.1	1.2	1.2	-6.2	2.67	2.66	0.3
28	1739	1742	-0.2	978.588	1141.69	-13.2	1.5	1.7	-11.7	2.84	2.82	0.6
32	1741	1749	-0.5	815.49	1141.69	-30.4	1.7	2.4	-27.2	3.08	2.95	4.7
36	1743	1758	-0.9	652.392	1196.05	-46.1	2.1	3.4	-39.7	3.4	3.18	7.0
40	1749	1762	-0.9	652.392	1032.95	-35.8	2.8	3.5	-19.0	3.59	3.4	5.4

is likely due to the onset of hole multiplication as we will see in this section. As discussed in section 1.1, many models describing impact ionization use a threshold energy below which no impact ionization occurs (see eg. [83]). This threshold is apparent for example in equation (1.2), and may be a 'soft' threshold, meaning that even below the ionization threshold some ionization occurs, due to the statistical nature of the process. From equation (1.4) it follows that, when the threshold field for hole multiplication is reached, higher gains will be observed, due to a non-zero k. The number of carriers reaching the threshold energy is itself temperature dependent through the Boltzmann equation. At temperatures above about 28°C, the distinction between the two slope regions is less clear. At these temperatures, hole multiplication may only start to occur at higher bias voltages, or it is quenched by the overabundance of phonons. We did not attempt to bias the modules to higher values than those presented in this paper because we wanted to keep the leakage current below 4 μA in order to reduce the risk of device failure.

Figure 20 clarifies the origin of the 'double exponential' observed in the gain and leakage current data. The red line is a three parameter fit according to equation (1.3):

$$M = \frac{(1-p_2)\, e^{(1-p_2)\left(p_0 e^{-\frac{p_1 W}{2V_b}}\right)}}{1-p_2 e^{(1-p_2)\left(p_0 e^{-\frac{p_1 W}{2V_b}}\right)}}, \tag{4.1}$$

where as before the bias voltage dependence of $k = p_2$ and $W = 125\ \mu m$ are ignored. The fit is underdetermined due to the correlation between the parameters. Nonetheless a good description of the data is obtained. Parameters $p_2 = k = 1.21 \cdot 10^{-3}$ and $p_1 = 1.32 \cdot 10^6$ are in good agreement with values from [31, 33]. $p_0 = aL = 8.07 \cdot 10^2$, taking $a = 3 \cdot 10^5$ [33], we obtain $L \approx 25 \mu m$, the

2012 JINST 7 P08001

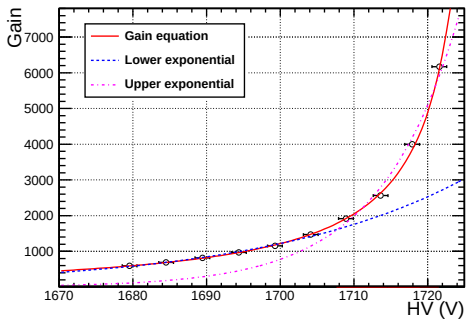

Figure 20. Gain as a function of bias voltage at 5°C. The red full line is a fit of equation (1.3) to the data, the dashed line is a fit to the lower gain region, corresponding to $k = 0$ in equation (1.4). Dash dotted line is a fit to the higher gain region.

distance across which avalanche multiplication occurs. Because of the assumed simplification and the underdetermined fit, only the order of magnitude of the presented results is important here, not the exact values. The values are in line with what is expected.

Figure 20 also presents the fits to the lower and upper gain region. It now becomes clear that the lower gain region corresponds to the region where $k = 0$ in equation (1.4). For non-zero k, the same equation demands additional terms to describe the gain. It also shows that describing the high gain region with a single exponential is a simplification. Indeed, the magenta dash-dotted line in the figure does not fit the data perfectly. Another observation is that in our simplified model, breakdown can't be reached if $k = 0$ due to the lack of a vertical asymptote for a single exponential function. In other devices, where the simplifications used here do not apply, breakdown may occur even when only electrons undergo impact ionization. A discussion on this topic is beyond the scope of this paper. See for instance [34].

The signal arrival time as measured by the TAC (figure 8) also shows a distinct region for lower and higher bias voltage. The difference in arrival time is caused by a different pulse shape, and thus on different CFD triggering time. Hole multiplication will affect pulse shapes. At higher temperatures, the differences are more linear.

As seen in equation (1.5), the excess noise factor increases as kM for high gain values. Since k is of $\mathcal{O}(10^{-3})$ in our device, the term kM will start to dominate for gains above 10^3, hence the decreased energy and time resolution at higher bias voltage is observed, even without hole multiplication. In addition, the onset of hole multiplication will result in a higher k_{eff}, causing a higher excess noise factor (equation (1.5)). In a similar device as the one under study, an increased k was observed for gains greater than $3 \cdot 10^3$ [39]. Figure 7 indeed shows a steep degradation in energy resolution at the highest voltages. The intersection method succeeds at predicting the bias voltage at which kM becomes the dominating contribution to the excess noise factor.

The higher excess noise factor also explains the deterioration in time resolution and flood histogram quality, seen in figures 13 and 14. The degradation is worse at lower temperatures than at higher ones, confirming the greater contribution of hole multiplication at lower temperatures.

2012 JINST 7 P08001

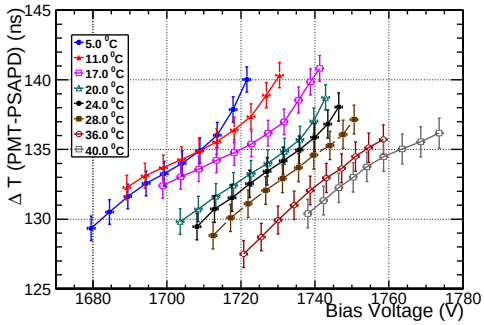

Figure 21. Difference in arrival time between signals coming from the PMT and the PSAPD for various PSAPD temperatures as a function of bias voltage. For visibility, data points are connected by a line.

Energy resolution does not improve much with temperature, only 1.25 percentage points between 40°C and 5°C, showing that the LSO crystal is the dominating contribution to the energy resolution (equation (1.8)) as also mentioned in section 1.1.3. The signal to noise ratio for APDs ($I_{\text{sig}} \cdot M/\sqrt{\text{eq. (1.6)}}$) suggests an optimal gain for which the signal-to-noise ratio is maximum. The optimal gain is dependent on the signal magnitude and may be much lower than the gains obtained in this work, as argued by [42][3] and for instance observed by [84].

From figure 15, time resolution improves from 3.4 ns to 2.4 ns between 40°C and 17°C, beyond which it does not further improve. The lack of improvement for temperatures below 17°C is due to the PMT contribution, since pulser measurements show that electronic noise decreases at lower temperatures and also because the width of the crystal peaks decreases below 17°C.

Even though fitting the time resolution data smoothes variations due to statistics or experimental uncertainties, it also introduces a potential danger of over-smoothing. We have ignored systematic uncertainties in this work. These include errors due to the various fitting algorithms used to extract the presented results as well as influences of external noise sources and errors in the temperature and leakage current readings.

Despite these limitations the time resolution is an excellent observable to assess the optimal bias voltage at different temperatures due to its significant dependence on bias voltage: the time resolution increases as a function of bias voltage due to decreased noise, decreased junction capacitance, and increased saturation velocity. At higher voltage the increased excess noise factor causes the time resolution to degrade.

Finally, it should be noted that the properties of the PSAPD itself will be more precisely determined when not coupled to a scintillation crystal array, because of the resolution blurring caused by the scintillator. A calibrated laser or an X-ray source could be used to irradiate the PSAPD directly. This method is in particular better for investigating properties such as k_{eff}, device gain and hole multiplication. Such a study is outside of the scope of this work as our goal is to characterize performance of the PSAPD in combination with the LSO crystal array.

[3]Note that these authors ignore the contribution of the scintillator.

2012 JINST 7 P08001

5 Conclusion

We present measurements of leakage current, gain, time resolution and flood histogram quality for an 8×8 array of $0.915 \times 0.915 \times 1.0$ mm^3 LSO crystals coupled to a PSAPD at temperatures varying between 5°C and 40°C. Lower temperatures yield superior performance. The increased excess noise factor and the onset of hole multiplication at high bias voltages degrades all important observables.

Different methods to predict the optimal bias voltage at each temperature are presented. From a practical point of view it is hard to use time resolution as an estimator of optimal bias voltage, since it requires a relatively slow coincidence acquisition and a radioactive source. A more practical method involves analyzing the width of the peaks observed in the crystal flood histogram, which follow a similar behavior as the time resolution. This method has the disadvantage that a large amount of data and a radioactive source are needed. By far the most practical method is the leakage current intersection method, since no source is required. Up to 28°C, the leakage current method agrees well with the predictions of the time resolution method.

Due to their exponential dependence on bias voltage, the exact values of the optimal gain and leakage current differ quite significantly even though their optimal bias voltage prediction only differs by a few Volts (see table 2). However, results suggest an optimal gain around 1500 (peak at 2.2 V) at all measured temperatures. Time resolution degrades by 10 % within ± 15 V of the optimal bias voltage. The window of about 30 V over which performance does not significantly degrade relaxes the requirements on the accuracy of the bias voltage selection.

At optimal bias voltage, the energy resolution degrades as $(10.5 \pm 0.1) + (0.038 \pm 0.006) \cdot T\,\%$. Coincidence time resolution stays constant at 2.37 ± 0.02 ns below 15°C. Above this temperature, time resolution deteriorates as $(1.67 \pm 0.06) + (0.042 \pm 0.002) \cdot T$ ns, and the FOM decreases by 0.11 ± 0.02 $\frac{1}{^\circ C}$. Even at high temperatures, all 64 peaks are still clearly visible in the flood histogram. The width of the peaks in the flood histogram show a quadratic degradation with temperature: $(2.6 \pm 0.1) \cdot 10^{-2} + (1.6 \pm 0.2) \cdot 10^{-5} \cdot T^2$.

A temperature gradient of 4°C is expected across the detector panels in the breast PET camera under development in our lab. In order to maintain a constant gain, a voltage adjustment of 1.70 ± 0.04 $\frac{\mathrm{V}}{^\circ \mathrm{C}}$ is needed. In order to obtain superior performance, the voltage needs to be increased by 1.64 ± 0.07 V for every degree decrease of temperature change. Both adjustments are similar, indicating that we can maintain optimal performance at comparable gains over a temperature range between 5°C and 40°C.

Acknowledgments

The authors would like to thank J. Lee for supportive work with the cooling setup, F.W.Y. Lau, P.D. Olcott and V.C. Spanoudaki from Stanford University and R. Farrell from RMD, inc for suggestions and fruitful discussions.

This work was supported by NIH grants R01 CA119056, R01 CA119056-S1 (ARRA), DOD grant W81XWH-10-1-0393, and the Stanford Physics Summer Research Program.

2012 JINST 7 P08001

References

[1] D. McElroy et al., *Characterization and readout of MADPET-II detector modules: validation of a unique design concept for high resolution small animal PET*, *IEEE Trans. Nucl. Sci.* **52** (2005) 199.

[2] B.J. Pichler et al., *Performance test of an LSO-APD detector in a 7 T MRI scanner for simultaneous PET/MRI*, *J. Nucl. Med.* **47** (2006) 639.

[3] M. Bergeron et al., *Performance evaluation of the LabPET APD-based digital PET scanner*, *IEEE Trans. Nucl. Sci.* **56** (2009) 10.

[4] E. Roncali et al., *Application of silicon photomultipliers to Positron Emission Tomography*, *Ann. Biomed. Eng.* **39** (2011) 1358.

[5] J. Zhang et al., *Study of the performance of a novel 1 mm resolution dual-panel PET camera design dedicated to breast cancer imaging using Monte Carlo simulation*, *Med. Phys.* **34** (2007) 689.

[6] F.W.Y. Lau et al., *1 mm^3 resolution breast-dedicated PET system*, *IEEE Nucl. Sci. Symp. Conf. Rec.* (2008) 5619.

[7] A.M.K. Foudray, *Design of an advanced Positron Emission Tomography detector system and algorithms for imaging small animal models of human disease*, Ph.D. thesis, University of California, San Diego U.S.A. (2008).

[8] A. Vandenbroucke et al., *Performance characterization of a new high resolution PET scintillation detector*, *Phys. Med. Biol.* **55** (2010) 5895.

[9] C.S. Levin et al., *Investigation of position sensitive avalanche photodiodes for a new high-resolution PET detector design*, *IEEE Trans. Nucl. Sci.* **51** (2004) 805.

[10] C.S. Levin, *New imaging technologies to enhance the molecular sensitivity of Positron Emission Tomography*, *Proc. IEEE* **96** (2008) 439.

[11] Y. Gu et al., *Effects of multiple-interaction photon events in a high-resolution PET system that uses 3D positioning detectors*, *Med. Phys.* **37** (2010) 5494.

[12] V.C. Spanoudaki et al., *Physical effects of mechanical design parameters on photon sensitivity and spatial resolution performance of a breast-dedicated PET system*, *Med. Phys.* **37** (2010) 5838.

[13] M.C. Abreu et al., *Design and evaluation of the clear-PEM scanner for Positron Emission Mammography*, *IEEE Trans. Nucl. Sci.* **53** (2006) 71.

[14] V. Spanoudaki et al., *Effect of temperature on the performance of proportional APD-based modules for gamma ray detection in Positron Emission Tomography*, *IEEE Trans. Nucl. Sci.* **55** (2008) 469.

[15] K.C. Burr et al., *Evaluation of a position sensitive avalanche photodiode for PET*, *IEEE Trans. Nucl. Sci.* **50** (2003) 792.

[16] S. St James et al., *Experimental characterization and system simulations of depth of interaction PET detectors using 0.5 mm and 0.7 mm LSO arrays*, *Phys. Med. Biol.* **54** (2009) 4605.

[17] Y. Wu et al., *A study of the timing properties of position-sensitive avalanche photodiodes*, *Phys. Med. Biol.* **54** (2009) 5155.

[18] S. Kim et al., *Phantom experiments on a PSAPD-based compact gamma camera with submillimeter spatial resolution for small animal SPECT*, *IEEE Trans. Nucl. Sci.* **57** (2010) 2518.

[19] M. McClish et al., *Performance measurements from LYSO scintillators coupled to a CMOS position sensitive SSPM detector*, *Nucl. Instrum. Meth.* **A 652** (2011) 264.

[20] C.R. Crowell et al., *Temperature dependence of avalanche multiplication in semiconductors*, *Appl. Phys. Lett.* **9** (1966) 242.

2012 JINST 7 P08001

[21] C. Jacoboni et al., *The Monte Carlo method for semiconductor device simulation*, Springer-Verlag, Wien Austria and New York U.S.A. (1989).

[22] R.J. McIntyre, *Multiplication noise in uniform avalanche diodes*, *IEEE Trans. Electr. Dev.* **13** (1966) 164.

[23] G.A. Baraff, *Distribution functions and ionization rates for hot electrons in semiconductors*, *Phys. Rev.* **128** (1962) 2507.

[24] K. Thornber, *Relation of drift velocity to low field mobility and high field saturation velocity*, *J. Appl. Phys.* **51** (1980) 2127.

[25] W. Shockley, *Problems related to p-n junctions in silicon*, *Solid State Electron.* **2** (1961) 35.

[26] P. Wolff, *Theory of electron multiplication in silicon and germanium*, *Phys. Rev.* **95** (1954) 1415.

[27] A.G. Chynoweth, *Uniform silicon p-n junctions. II. Ionization rates for electrons*, *J. Appl. Phys.* **31** (1960) 1161.

[28] C.A. Lee et al., *Ionization rates of holes and electrons in silicon*, *Phys. Rev.* **134** (1964) A761.

[29] R. Van Overstraeten et al., *Measurement of the ionization rates in diffused silicon p-n junctions*, *Solid State Electron.* **13** (1970) 583.

[30] M. Woods et al, *Use of a Schottky barrier to measure impact ionization coefficients in semiconductors*, *Solid State Electron.* **16** (1973) 381.

[31] W. Grant, *Electron and hole ionization rates in epitaxial silicon at high electric fields*, *Solid State Electron.* **16** (1973) 1189.

[32] J.W. Slotboom et al, *Surface impact ionization in silicon devices*, *IEEE Internat. Electron Dev. Meeting* **33** (1987) 494.

[33] W. Maes et al., *Impact ionization in silicon: a review and update*, *Solid State Electron.* **33** (1990) 705.

[34] R.J. McIntyre, *A new look at impact ionization — part I: a theory of gain, noise, breakdown probability, and frequency response*, *IEEE Trans. Electr. Dev.* **46** (1999) 1623.

[35] S.M. Sze, *Physics of semiconductor devices*, New York U.S.A. (1981).

[36] G. Petrillo et al., *Scintillation detection with large-area reach-through avalanche photodiodes*, *IEEE Trans. Nucl. Sci.* **31** (1984) 417.

[37] P.P. Webb, *Large area reach-through avalanche diodes for X-ray spectroscopy*, *IEEE Trans. Nucl. Sci.* **23** (1976) 138.

[38] C.M. Pepin et al., *New UV-enhanced, ultra-low noise silicon avalanche photodiode for radiation detection and medical imaging*, *IEEE Nucl. Sci. Symp. Conf. Rec.* (2010) 1740.

[39] R. Redus et al., *Gain and noise in very high-gain avalanche photodiodes: theory and experiment*, *Proc. SPIE* **2859** (1996) 288.

[40] R. Lecomte et al., *Performance characteristics of BGO-silicon avalanche photodiode detectors for PET*, *IEEE Trans. Nucl. Sci.* **32** (1985) 482.

[41] B.J. Pichler et al., *A* 4×8 *APD array, consisting of two monolithic silicon wafers, coupled to a* 32*-channel LSO matrix for high-resolution PET*, *IEEE Trans. Nucl. Sci.* **48** (2001) 1391.

[42] R. McIntyre et al., *A short-wavelength selective reach-through avalanche photodiode*, *IEEE Trans. Nucl. Sci.* **43** (1996) 1341.

2012 JINST 7 P08001

[43] R. Lecomte et al., *Investigation of GSO, LSO and YSO scintillators using reverse avalanche photodiodes*, *IEEE Trans. Nucl. Sci.* **45** (2002) 478.

[44] G.C. Huth et al., *Stable, high field silicon p-n junction radiation detectors*, *Rev. Sci. Instrum.* **34** (1963) 1283.

[45] R.J. Locker et al., *A new ionizing radiation detection concept which employs semiconductor avalanche amplification and the tunnel diode element*, *Appl. Phys. Lett.* **9** (1966) 227.

[46] R. Farrell et al., *Large area silicon avalanche photodiodes for scintillation detectors*, *Nucl. Instrum. Meth.* **A 288** (1990) 137.

[47] M. Moszyski et al., *Large area avalanche photodiodes in scintillation and X-rays detection*, *Nucl. Instrum. Meth.* **A 485** (2002) 504.

[48] R. Farrell et al., *APD arrays and large-area APDs via a new planar process*, *Nucl. Instrum. Meth.* **A 442** (2000) 171.

[49] M.J. Paulus et al., *Comparison of the beveled-edge and reach-through APD structures for PET applications*, *IEEE Nucl. Sci. Symp. Conf. Rec.* **4** (1994) 1864.

[50] M. McClish et al., *A study of low resistivity, deep diffused, silicon avalanche photodiodes coupled to a $LaBr_3$:Ce scintillator*, *Nucl. Instrum. Meth.* **A 610** (2009) 207.

[51] M. McClish et al., *A reexamination of deep diffused silicon avalanche photodiode gain and quantum efficiency*, *IEEE Trans. Nucl. Sci.* **53** (2006) 3049.

[52] R. Lecomte et al., *Status of BGO-avalanche photodiode detectors for spectroscopic and timing measurements*, *Nucl. Instrum. Meth.* **A 278** (1989) 585.

[53] R. Lecomte et al., *Investigation of GSO, LSO and YSO scintillators using reverse avalanche photodiodes*, *IEEE Trans. Nucl. Sci.* **45** (1998) 478.

[54] M. Moszynski et al., *Energy resolution of scintillation detectors readout with large area avalanche photodiodes and photomultipliers*, *IEEE Trans. Nucl. Sci.* **45** (1998) 472.

[55] S.A. Payne et al., *Nonproportionality of scintillator detectors: theory and experiment. II*, *IEEE Trans. Nucl. Sci.* **58** (2011) 3392.

[56] M. Balcerzyk et al., *YSO, LSO, CSO and LGSO. A study of energy resolution and nonproportionality*, *IEEE Trans. Nucl. Sci.* **47** (2000) 1319.

[57] H. Spieler, *Fast timing methods for semiconductor detectors*, *IEEE Trans. Nucl. Sci.* **29** (1982) 1142.

[58] R. Lecomte et al., *Radiation detection measurements with a new "Buried Junction" silicon avalanche photodiode*, *Nucl. Instrum. Meth.* **A 423** (1999) 92.

[59] Y. Varshni, *Temperature dependence of the energy gap in semiconductors*, *Physica* **34** (1967) 149.

[60] C. Thurmond, *The standard thermodynamic functions for the formation of electrons and holes in Ge, Si, GaAs, and GaP*, *J. Electrochem. Soc.* **122** (1975) 1133.

[61] C. Canali et al., *Measurements of the average energy per electron-hole pair generation in silicon between* 5–320 *K*, *IEEE Trans. Nucl. Sci.* **19** (1972) 9.

[62] R.C. Alig et al., *Scattering by ionization and phonon emission in semiconductors*, *Phys. Rev.* **B 22** (1980) 5565.

[63] D.R. Decker et al., *Temperature dependence of carrier ionization rates and saturated velocities in silicon*, *J. Electron. Mater.* **4** (1975) 527.

2012 JINST 7 P08001

[64] P. Mars, *Temperature dependence of avalanche breakdown voltage in p-n junctions*, *Internat. J. Electron.* **32** (1972) 23.

[65] M. Ershov et al., *Temperature dependence of the electron impact ionization coefficient in silicon*, *Semicond. Sci. Technol.* **10** (1995) 138.

[66] S. Selberherr, *MOS device modeling at liquid-nitrogen temperature*, *IEEE Trans. Electr. Dev.* **36** (1989) 1464.

[67] Y. Okuto et al., *Ionization coefficients in semiconductors: a nonlocalized property*, *Phys. Rev.* **B 10** (1974) 4284.

[68] S. Reggiani et al., *Measurement and modeling of the electron impact-ionization coefficient in silicon up to very high temperatures*, *IEEE Trans. Electr. Dev.* **52** (2005) 2290.

[69] C. Jacoboni et al., *A review of some charge transport properties of silicon*, *Solid State Electron.* **20** (1977) 77.

[70] C. Canali et al., *Electron drift velocity in silicon*, *Phys. Rev.* **B 12** (1975) 2265.

[71] J.D. Naud et al., *The role of cerium sites in the scintillation mechanism of LSO*, *IEEE Trans. Nucl. Sci.* **43** (1996) 1324.

[72] P. Szupryczynski et al., *Thermoluminescence and scintillation properties of rare earth oxyorthosilicate scintillators*, *IEEE Trans. Nucl. Sci.* **51** (2004) 1103.

[73] K. Shah et al., *Position-sensitive avalanche photodiodes for gamma-ray imaging*, *IEEE Trans. Nucl. Sci.* **49** (2002) 1687.

[74] F.W.Y. Lau et al., *Analog signal multiplexing for PSAPD-based PET detectors: simulation and experimental validation*, *Phys. Med. Biol.* **55** (2010) 7149.

[75] M. Moszynski et al., *Characterization of scintillators by modern photomultipliers — a new source of errors*, *IEEE Trans. Nucl. Sci.* **57** (2010) 2886.

[76] C. Moisan et al., *DETECT*2000*: the object oriented C++ language version of DETECT*, Dept. of Electrical Engineering, Laval University, Quebec Canada (2000).

[77] A. Vandenbroucke et al., *Effects of external shielding on the performance of a* 1 mm^3 *resolution breast PET camera*, *IEEE Nucl. Sci. Symp. Conf. Rec.* (2010) 3644.

[78] R. Brun et al., *ROOT: an object oriented data analysis framework*, *Nucl. Instrum. Meth.* **A 389** (1997) 81.

[79] J. Zhang et al., *A new positioning algorithm for position-sensitive avalanche photodiodes*, *IEEE Trans. Nucl. Sci.* **54** (2007) 433.

[80] C.M. Pepin et al., *Properties of LYSO and recent LSO scintillators for phoswich PET detectors*, *IEEE Trans. Nucl. Sci.* **51** (2004) 789.

[81] C.L. Melcher et al., *Scintillation properties of LSO:Ce boules*, *IEEE Trans. Nucl. Sci.* **47** (2000) 965.

[82] P.D. Reynolds et al., *Convex optimization of coincidence time resolution for high resolution PET systems*, *IEEE Trans. Med. Imag.* **30** (2011) 391.

[83] Y.W. Chen et al., *Impact ionization coefficient and energy distribution function at high fields in semiconductors*, *J. Appl. Phys.* **65** (1989) 4279.

[84] L. Ludhova et al., *Planar LAAPDs: temperature dependence, performance and application in low energy X-ray spectroscopy*, *Nucl. Instrum. Meth.* **A 540** (2005) 169 [physics/0410099].

2012 JINST 7 P08001